

## Experimental observation of topological transition in linear and nonlinear parametric oscillators

Benjamin Apffel<sup>1</sup>\* and Romain Fleury<sup>2</sup>

*Institute of Electrical and Micro Engineering, Laboratory of Wave Engineering, Ecole Polytechnique Fédérale de Lausanne (EPFL), Station 11, 1015 Lausanne, Switzerland*

 (Received 2 October 2023; accepted 5 April 2024; published 10 May 2024)

Parametric oscillators are examples of externally driven systems that can exhibit two stable states with opposite phase depending on the initial conditions. In this work, we propose to study what happens when the external forcing is perturbed by a continuously parametrized defect. Initially in one of its stable states, the oscillator will be perturbed by the defect and finally reach another stable state, which can be its initial one or the other one. For some critical value of the defect parameter, the final state changes abruptly. We theoretically and experimentally investigate such transition both in the linear and nonlinear cases, and the effect of nonlinearities is discussed. A topological interpretation in terms of winding number is proposed, and we show that winding changes correspond to singularities in the temporal dynamics. An experimental observation of such transition is performed using parametric Faraday instability at the surface of a vibrated fluid.

DOI: [10.1103/PhysRevE.109.054204](https://doi.org/10.1103/PhysRevE.109.054204)

### I. INTRODUCTION

The parametric oscillator is one of the simplest externally driven systems, a paradigmatic example being a pendulum shaken vertically at twice its resonance frequency. Parametric oscillators are encountered in many different fields of physics, including quantum mechanics [1–3], optics [4,5], (micro)mechanics [6–9], electronics [10], and hydrodynamics [11,12], making their study of prime interest. The rich physics of this system results from complex interactions between damping, forcing, and nonlinearity. The response amplitude of the system strongly depends on the exact parameters of the system and can exhibit (among others) linear stability around zero, subcritical or supercritical Hopf bifurcation toward a finite amplitude oscillation, subharmonic oscillation, bistability, and hysteresis [12,13]. For a given configuration, the amplitude response when the external forcing is perturbed has also been investigated recently in the context of time crystals [14,15].

In parallel to the amplitude behavior, the phase response of the system has also been investigated in several regimes. In the linearly stable regime, it can, for instance, be used to perform squeezing of noise in thermal [8] and quantum [2,3] regimes. In the subharmonic finite amplitude oscillation regime, the oscillation phase is fixed by the forcing and can only take two discrete values separated by  $\pi$ . This phase degeneracy has, for instance, been used as an analog bit to store information [16,17] or to simulate the two states of a 1/2-spin in coherent Ising machines to compute the ground state of the Hamiltonians [18–22]. In this context, several strategies to perform bit flipping (or phase switch) have been implemented by perturbing the excitation signal in a specific

manner [23,24]. Possible bifurcation between several stable states in the presence of noise has also been investigated in the context of chaos control [25–27].

The purpose of the present work is to study the condition for a phase switch to occur by considering a continuously parametrized family of perturbations (or time defects), rather than random noise or specific perturbations. The continuous parameter will generate a family of trajectories which will display strong discontinuities at specific values of the parameter. The paper is organized as follows. We first introduce some useful formalism to study linear parametric oscillators and define our family of time defects. We then show that there exists some critical values of the parameter that separate no phase-switch to phase-switch behavior, giving rise to a transition with respect to the defect parameter. Interestingly, we show that this transition exhibits topological properties and provide experimental observation of such transition. We then introduce some nonlinearity and discuss its impact theoretically, numerically, and experimentally on the transition process.

### II. PARAMETRIC OSCILLATOR AND TEMPORAL DEFECT

#### A. Parametric oscillation and averaging equation

Here, we first describe the key features of parametric oscillation and phase selection. We consider, as in Fig. 1(a), a pendulum with natural pulsation  $\omega$  and vibrated at  $2\omega$ . For now, we will not consider nonlinear effects and the evolution equation for the angular coordinate  $\psi$  is then

$$\frac{d^2\psi}{dt^2} + \frac{2}{\tau} \frac{d\psi}{dt} + \omega^2[1 + \epsilon \cos(2\omega t)]\psi = 0, \quad (1)$$

where  $\tau$  is the damping time and  $\epsilon$  is the adimensional forcing amplitude. We assume that the forcing, the damping, and the

\*benjamin.apffel@epfl.ch

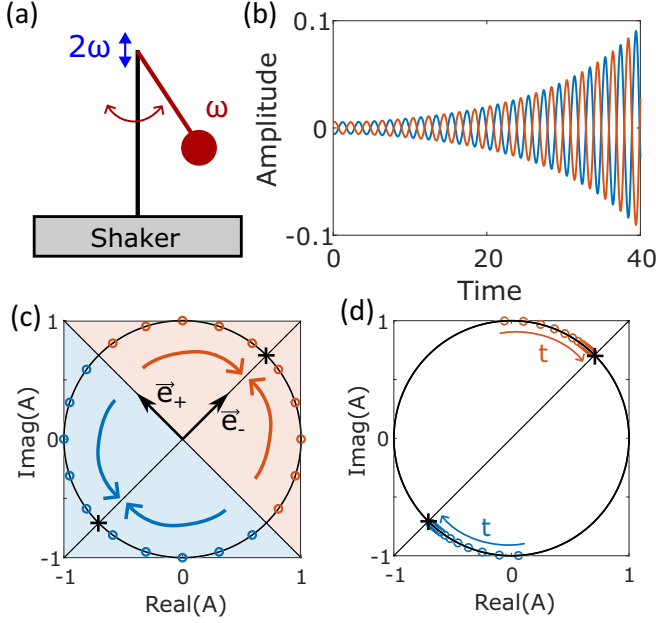


FIG. 1. Parametric oscillator and phase state. (a) An example of a parametric oscillator: a pendulum with natural pulsation of  $\omega$  vibrated at  $2\omega$ . (b) Angular position of the pendulum evolving according to Eq. (1) for  $\omega = \pi$ ,  $\epsilon = 0.03$ ,  $\omega\tau = 200$  and opposite initial conditions. Depending on the latter, two phases of the oscillation can be observed. (c) Diagram showing, for different initial conditions on the unit circle, which phase state is reached by the system at long time. The two regions are defined by  $\vec{A}_0 \cdot \vec{e}_- > 0$  (red) and  $\vec{A}_0 \cdot \vec{e}_- < 0$  (blue). (d) Normalized complex amplitude along time computed from (b). The oscillation phase converges toward one of the two fixed points as time flows.

initial condition are small:  $\epsilon \ll 1$ ,  $1/\omega\tau = \epsilon\gamma \ll 1$ ,  $\psi \ll 1$ ,  $\dot{\psi} = 0$ . For  $\gamma < 1/2$ , the angular position  $\psi(t)$  exponentially grows with a slow timescale while oscillating at  $\omega$ , as shown in the direct numerical simulation of Eq. (1) in Fig. 1(a). In order to discard the oscillation, we introduce the complex envelope  $A(t)$  as

$$\psi(t) = \text{Re}[A(t)e^{i\omega t}], \quad \dot{\psi}(t) = -\omega \text{Im}[A(t)e^{i\omega t}]. \quad (2)$$

This envelope will evolve with a slow timescale,  $\sim \epsilon/\omega$  (see the Supplemental Material [28] or Ref. [29]), and carry information on the oscillation phase. If one identifies the complex amplitude  $A(t)$  with its corresponding vector  $\vec{A}$  in  $\mathbb{R}^2$ , it evolves according to

$$\partial_t \vec{A} = \frac{\partial}{\partial t} \begin{bmatrix} \text{Re}(A) \\ \text{Im}(A) \end{bmatrix} = -\epsilon \begin{bmatrix} \gamma/2 & -1/4 \\ -1/4 & \gamma/2 \end{bmatrix} \begin{bmatrix} \text{Re}(A) \\ \text{Im}(A) \end{bmatrix}. \quad (3)$$

The matrix admits two eigenvalues,  $\lambda_{\pm} = -\epsilon(\gamma/2 \pm 1/4)$ , with corresponding orthogonal eigenvectors,  $\vec{e}_{\pm} = [1; \mp 1]^T$ . If the damping is small enough ( $\gamma < 1/2$ ), one has  $\lambda_+ < 1 < \lambda_-$ . For the angular coordinate  $\psi(t)$ , three behaviors can therefore be observed when  $t \rightarrow \infty$  depending on the initial condition  $\vec{A}_0$ :

- (i) if  $\vec{A}_0 \cdot \vec{e}_- > 0$ ,  $\psi(t)$  exponentially grows while oscillating at  $\omega$  with phase  $\pi/4$ ,
- (ii) if  $\vec{A}_0 \cdot \vec{e}_- < 0$ ,  $\psi(t)$  exponentially grows while oscillating at  $\omega$  with phase  $\pi/4 + \pi$ , and

- (iii) if  $\vec{A}_0 \cdot \vec{e}_- = 0$ ,  $\psi(t)$  goes exponentially to zero.

Unless specific initial conditions are chosen and the system is completely free of noise, the last behavior is not seen and the generic behavior therefore exponentially grows combined with an oscillation which can only have two different phases. This twofold phase degeneracy is directly related to the 2:1 resonance between the forcing and the pendulum response combined with the invariance of the evolution equation under the discrete symmetry  $t \rightarrow t + \pi/\omega$ . One can also understand it geometrically: as the projection of  $\vec{A}_0$  on  $\vec{e}_+$  will be exponentially killed,  $\vec{A}$  will tend to align or anti-align with  $\vec{e}_-$ . The choice of one phase or the other is therefore determined by the sign of the projection between the initial condition and the growing eigenvector,  $\vec{A}_0 \cdot \vec{e}_-$ , as shown in Fig. 1(c). The degeneracy is illustrated in Fig. 1(b), where we perform a direct simulation of Eq. (1) with the same forcing, but opposite initial conditions. As everything is linear, it is enough to consider the normalized amplitude  $\tilde{A} = A(t)/|A(t)|$ . Its evolution is shown in Fig. 1(d) and its convergence toward one of the two “phase states” is visible.

## B. Introducing a continuously parameterized perturbation and qualitative analysis of its impact

Let us now assume that the forcing amplitude is fixed and that the parametric oscillator has reached one of its phase states. We now perturb the forcing of the system by detuning between  $t = 0$  and  $t = T_{\lambda} = \pi/\omega|\lambda|$  the excitation frequency from  $2\omega$  to  $2\omega(1 + \lambda)$ , with all other parameters left unchanged. Doing so, the perturbed excitation takes an overall phase of  $\pm 2\pi$  (depending on the sign of the detuning  $\lambda$ ) compared to the unperturbed signal, as shown in Fig. 2(a). After  $T_{\lambda}$ , the perturbed excitation is back in phase with the unperturbed one and the excitation frequency is set back to  $2\omega$ . This particular choice of  $T_{\lambda}$  ensures (1) the continuity of the excitation signal as shown in Fig. 2(a) and (2) that the possible phase states of the oscillator are the same before and after the defect, since they are completely determined by the phase of the forcing. Equivalently, this condition ensures that the eigenvectors for the envelope equation are the same before and after the defect.

Here, we briefly describe qualitatively what one would expect by introducing such perturbation. The latter can be seen as a continuous phase sweep of the external forcing from 0 to  $\pm 2\pi$  at speed  $2\omega|\lambda|$ . If the sweep is very fast ( $\lambda \gg 1$ ), one expects the oscillator not to be significantly perturbed by the phase sweep. In particular, the oscillator’s phase should remain close to the one of an unperturbed oscillator. On the other hand, if the sweep is very slow ( $\lambda \ll 1$ ), one expects the phase of the oscillator to be locked with the forcing’s phase at each time. Due to period doubling of the oscillator compared to the forcing, the sweep of  $\pm 2\pi$  of the latter will lead to a phase switch of  $\pm \pi$  in the former. From here, we see that depending on the value of  $\lambda$ , the oscillator will or will not experience a phase switch. The next sections aim to derive a condition on  $\lambda$  for such switch to occur and understand what happens at the particular values of  $\lambda$  at which the dynamic of the system suddenly changes from no phase switch to a phase switch.

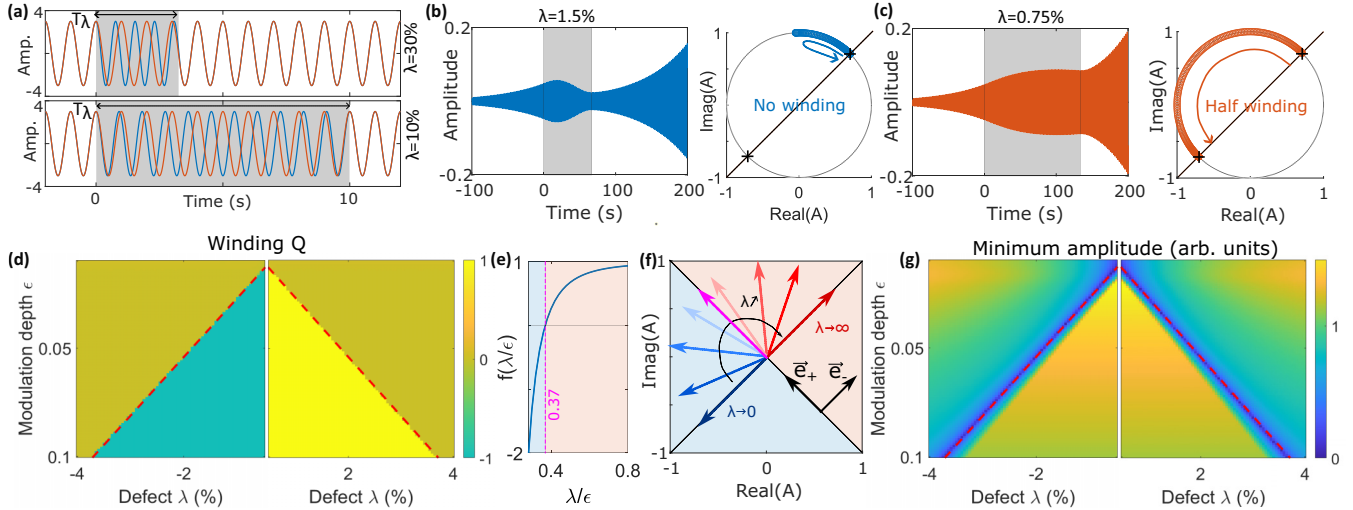


FIG. 2. Temporal defect, phase state switch, and topological aspect of transition in the linear case. (a) Two examples of defects (blue curves) for  $\lambda = 30\%$  (top) and  $\lambda = 10\%$  (bottom), the unperturbed excitation being plotted for comparison in red. The duration of the detuning is chosen so that the two excitation signals collapse back together after  $T_\lambda$ . (b) Simulated evolution of the parametric oscillator for  $\epsilon = 0.03$ ,  $\lambda = 1.5\%$  and (c)  $\lambda = 0.75\%$ , with the gray area corresponding to the defect duration. The phase of the corresponding complex amplitude is also shown and the phase switch only occurs for the second case. (d) Half-winding  $Q$  of the normalized amplitude  $\tilde{A}(t)$  for different values of  $(\epsilon, \lambda)$ . The red dashed line corresponds to the analytical prediction  $\lambda/\epsilon = 0.37$ . (e) Analytical computation of  $\tilde{A}(T_\lambda) \cdot \tilde{e}_- = f(\lambda/\epsilon)$ , which cancels for  $\epsilon/\lambda = 0.37$ . (f) Normalized complex amplitude  $\tilde{A}(T_\lambda)$  when  $\lambda$  varies from 0 to infinity, with the initial amplitude  $\tilde{A}(0) = \tilde{e}_-$ . The transition from positive to negative (pink arrow) occurs for  $\lambda/\epsilon = 0.37$ . (g) Minimum amplitude of the field,  $\min_{t>0}|A(t)|$ , for different values of  $(\lambda, \epsilon)$ . The field cancels exactly when the winding changes.

### III. TRANSITION IN LINEAR PARAMETRIC OSCILLATOR

#### A. Discrete phase states vs continuous parameter

Adding this defect will perturb the parametric oscillator initially in one of its phase states (aligned or anti-aligned with  $\tilde{e}_-$ ). As everything is linear, let us assume, without loss of generality, that  $A(t=0) = \tilde{e}_-$ . During the defect, the evolution equation is modified so that  $\tilde{e}_\pm$  are no more eigenvectors for the evolution operator [28]. The exponential growth will be perturbed and  $\tilde{A}$  will start to move away from  $\tilde{e}_-$ , as shown in Figs. 2(b) and 2(c). After the defect, the system is in the state  $\tilde{A}(T_\lambda)$  and will, after some time, align or anti-align again with  $\tilde{e}_-$ . As discussed before, knowing which of the two occurs is fully determined by the sign of the geometrical projection,  $\tilde{A}(T_\lambda) \cdot \tilde{e}_-$ . The introduction of the defect can therefore be seen as a change in the initial condition, and varying the defect parameter  $\lambda$  as a continuous change of the initial conditions.

In agreement with the previous qualitative analysis, both phase switch and no phase switch can occur depending on the value of  $\lambda$ . This is shown in Figs. 2(b) and 2(c), where for the same forcing  $\epsilon = 0.03$ , a phase switch occurs for  $\lambda = 0.75\%$  but not for  $\lambda = 1.5\%$ . In order to characterize the phase difference between the initial and the final states, we define the number

$$Q(\lambda, \epsilon) = \frac{1}{\pi} \text{Im} \left( \ln \frac{A(\infty)}{A(0)} \right) \quad (4)$$

that counts the number of half winds around the origin, which must be an integer. The resulting transition diagram in the  $(\lambda, \epsilon)$  plane shows whether or not a phase switch occurs depending on the system parameters. Direct numerical

computation of the half-winding number  $Q(\lambda, \epsilon)$  is displayed in Fig. 2(d). It is constant on large domains that are separated by a curve of critical values of  $\lambda$  that can be fitted as  $\lambda_c = \alpha\epsilon$  with  $\alpha \approx 0.37$  (red line).

As discussed above, the transition is entirely driven by the sign of  $\tilde{A}(T_\lambda) \cdot \tilde{e}_-$ . An explicit computation using perturbative methods shows that if  $\tilde{A}(t=0) = \tilde{e}_-$ , one has  $\tilde{A}(T_\lambda) \cdot \tilde{e}_- = f(\lambda/\epsilon)$ , where  $f$  is plotted in Fig. 2(d) and explicitly given in the Supplemental Material [28]. In particular, it only cancels once for  $\lambda/\epsilon \approx 0.37$ , which exactly matches direct numerical simulation [see Fig. 2(e)]. Such analysis, moreover, provides a straightforward geometrical interpretation of the transition. For a given forcing  $\epsilon$ , the vector state  $\tilde{A}(T_\lambda)$  performs half a turn between  $\tilde{e}_-$  and  $-\tilde{e}_-$  when  $\lambda$  goes from 0 to  $\infty$ , as illustrated in Fig. 2(f). The transition between no phase shift and phase shift occurs at the critical value  $\lambda_c$  when the vector state becomes exactly orthogonal to  $\tilde{e}_-$ .

At this critical value, the projection cancels out and  $\tilde{A}(T_\lambda)$  is aligned with  $\tilde{e}_+$ . Accordingly, the parametric oscillator is expected to go exponentially fast to zero. This is confirmed by the diagram in Fig. 2(g) that shows the (normalized) minimum amplitude reached by the oscillator,  $\min_{t>0}|A(t)|$ . The amplitude therefore exactly cancels out when the winding change occurs.

#### B. Topological aspect of the transition

Such cancellation near the winding number change is reminiscent of what typically occurs in condensed matter during a topological phase transition. In this context, topological invariants are written as an integral over the reciprocal space [30–32]. If one writes  $A(t) = e^{i\phi(t)}$ , one can also write  $Q$  as an

integral, but it will rather run over the time dimension,

$$Q(\lambda) = \frac{1}{\pi} \int_0^\infty \dot{\phi} dt. \quad (5)$$

In terms of topology, the winding number  $Q$  characterizes the homotopy class of the path followed by the complex amplitude. The variation of  $\lambda$  can therefore be seen as the generation of a family of continuously parameterized trajectories in the complex plane. For particular values of  $\lambda$ , the homotopy class of the trajectory suddenly changes, corresponding to a discontinuity of path parametrization with respect to  $\lambda$ . This occurs when the field reaches the origin and cancels out. Topological transitions are usually associated with singularities. In the present case, it is the singular behavior of the dynamics at this specific value of  $\lambda$  that plays this role. Indeed, the origin is an unstable equilibrium point, and it can therefore only be reached for very specific values of  $\lambda$ , while the generic behavior is to reach one of the two stable states (aligned, or anti-aligned with  $\vec{e}_-$ ).

One can push the analogy with topological transitions a bit further. A phase transition in condensed matter is typically associated with the divergence of some correlation length at the transition. In our case, such length is replaced by the typical convergence time  $T_c$  taken by  $\dot{A}(t)$  to approximately align again with  $\vec{e}_-$ . Close from the critical value  $|\lambda - \lambda_c| \ll 1$ , one expects  $T_c \sim \ln|\lambda - \lambda_c|$ . This scaling has been verified numerically [see Sec. IV A and Fig. 4(c)], and one therefore finds an exponential scaling law rather than a power law with some critical exponents in condensed matter.

### C. Experimental observation

We now propose an experimental observation of such transition between different homotopy classes. As a parametric oscillator, we chose the Faraday waves that occur at the surface of a vibrated fluid [12]. For small deformation of the interface, the governing equation for the height field  $h_k$  associated to wave vector  $k$  at the surface of a vibrated fluid with acceleration  $a \cos(2\omega t)$  is [12]

$$\partial_t h_k + \frac{1}{\tau} \partial_t h_k + [gk + \gamma k^3 / \rho + ak \cos(2\omega t)] h_k = 0, \quad (6)$$

where  $\tau$  accounts for viscous dissipation and is measured experimentally to be  $\tau = 0.9 \pm 0.03$  s,  $g = 9.8$  m/s<sup>2</sup> is local gravity,  $\gamma = 60$  mJ/m<sup>2</sup> is the surface tension of water, and  $\rho = 1000$  kg/m<sup>3</sup> is water density. From this, we can therefore estimate the adimensional forcing as

$$\epsilon = \frac{ak}{gk + \gamma k^3 / \rho}. \quad (7)$$

The experimental setup consists of a tank of water vibrated at  $2\omega$  using a shaker. In order to avoid friction of the parametrically excited waves on the walls, a plastic frame pierced in its center by a square hole of  $2 \times 2$  cm is placed at the surface, as shown in Fig. 3(a). The frame is floating on the water so that evaporation of water does not change the boundary condition of the meniscus, which could impact the experiments [12, 14]. The first mode of the square hole is measured to occur at  $7.92 \pm 0.02$  Hz (see the Supplemental Material [28]) and we therefore fix the excitation frequency to 15.84 Hz, which

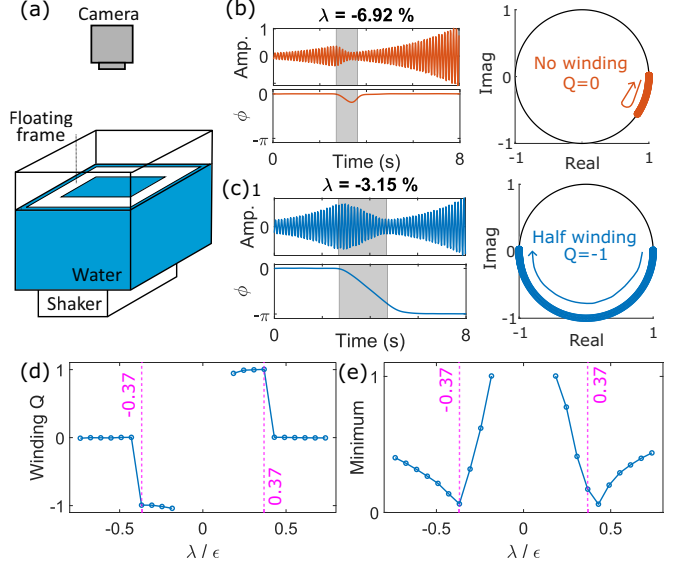


FIG. 3. Experimental measurement of phase state switch in the linear regime. (a) Sketch of the experimental setup: A tank filled with water is placed on a shaker vibrating at 15.92 Hz. A floating frame at the surface ensures a good definition of the first parametrically unstable mode at 7.92 Hz. A camera on the top recovers the wave amplitude through demodulation of a periodic pattern placed below the surface (not shown here). (b),(c) Typical experimental signal for the wave amplitude (in arbitrary units) and the slowly varying phase for (b)  $\lambda = -6.92\%$  and (c)  $\lambda = -3.15\%$ . In both cases, the forcing is  $\epsilon = 0.10$  and the defect occurs at  $t \approx 4$ s. Half-negative winding occurs in the second case, but not in the first one. (d) Half-winding number  $Q(\lambda)$  and (e) minimum amplitude for different values of  $\lambda$  plotted as a function of  $\lambda/\epsilon$ . The vertical lines show the theoretical prediction for the transition  $\lambda_c/\epsilon = 0.37$ .

corresponds to  $k \approx 200$  m<sup>-1</sup>. The instability threshold is found for a critical acceleration of  $a_c \approx 1.4$  m/s<sup>2</sup> corresponding to  $\epsilon \approx 0.11$ . In this case, we observe waves at half the excitation frequency that exponentially grows for typically 15 s before saturating at finite amplitude due to nonlinearity. As we aim to probe the linear regime, each experiment consists of 7 s of unperturbed excitation, a defect parametrized by  $\lambda$ , and, finally, 8 s of unperturbed excitation again, before stopping the vibration and letting the system come back to rest for the next measurement. Such procedure ensures that the wave amplitude remains far from its nonlinear saturation. The wave amplitude is recovered by a camera placed above the water and a periodic pattern placed below the surface. Using a demodulation algorithm, one can retrieve the surface deformation through the pattern distortion recorded by the camera [33].

Some typical wave amplitude measurements along time are shown in Figs. 3(b) and 3(c) with  $\lambda = -6.92\%$  and  $\lambda = -3.15\%$ , respectively. From these curves, one can compute the phase and the corresponding winding in the complex plane, as shown in the same panels. Depending on the value of  $\lambda$ , the trajectory either performs half-negative, half-positive, or no winding around the origin of the complex plane. Figure 3(d) shows the value of the winding index  $Q$  for different values of  $\lambda$ , the forcing fixed to  $\epsilon = 0.10$ . In order to compare



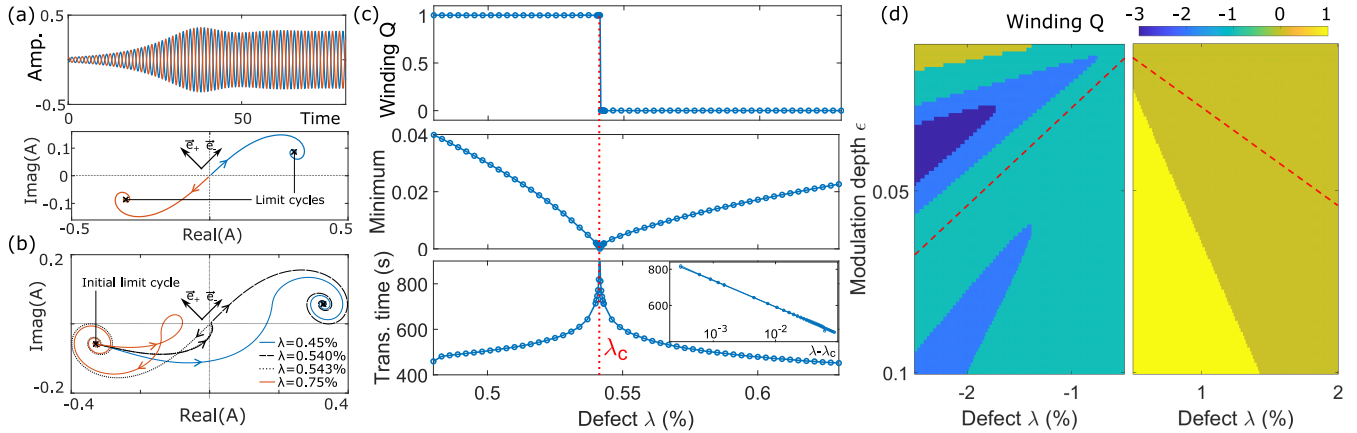


FIG. 4. Impact of nonlinearity on the transition process. (a) Upper panel: angular position along time simulated from nonlinear evolution with  $\omega = \pi$ ,  $\epsilon = 0.03$ ,  $\omega\tau = 200$  for opposite initial conditions. Depending on the initial condition, two phases for the oscillation can be observed. Lower panel: associated complex amplitude that reaches a fixed point corresponding to one of the two limit cycles. (b) Trajectories in the complex plane for  $\epsilon = 0.03$  and defect parameters  $\lambda = 0.45, 0.540, 0.543, 0.6\%$  when the system is initially in one of its limit cycles. The two convergence points of the trajectories are the two possible limit cycles with opposite phase. (c) Half-winding index  $Q$  (top), minimum amplitude along time,  $\min_{t>0}|A(t)|$  (middle), and time of convergence,  $T_c$  (bottom), as a function of  $\lambda$ . Inset: Same plot with logarithmic horizontal axis to test  $T_c \sim \ln|\lambda - \lambda_c|$ . (d) Transition diagram  $Q(\epsilon, \lambda)$  for the nonlinear case. The red-dashed line corresponds to the prediction from the linear case.

our results with the theory, we normalize the horizontal axis by  $\epsilon$ . The resulting curve is antisymmetric with respect to  $\lambda/\epsilon$ , as expected from theory and numerical simulations. Moreover, the transition occurs for a specific value of  $\lambda/\epsilon$  that is consistent with the theoretical prediction,  $\lambda_c/\epsilon = \pm 0.37$ . We also compute the minimum amplitude of the waves normalized by the maximal amplitude before the defect and the result is shown in Fig. 3(e). The transition between different winding numbers indeed corresponds to an (almost) cancellation of the wave amplitude, which is again consistent with the prediction. Our experimental results also exhibit a clear increase of the transition time near the transition, but the exponential prediction could not be observed experimentally. We attribute this to the presence of noise at the water surface that prevents the observation of a very small amplitude of parametric waves for a very long time.

It is tempting to vary  $\epsilon$  in order to establish complete transition diagrams. However, as the latter increases, the system hits nonlinearities within a few seconds, preventing it from performing a measurement in the purely linear case. The next sections are dedicated to discuss the role of nonlinearities, theoretically and experimentally, in the transition process.

#### IV. IMPACT OF NONLINEARITY ON TRANSITION PROCESS

##### A. Nonlinear parametric oscillator

Realistically, all parametric oscillators will not grow exponentially forever, but will eventually saturate in amplitude due to nonlinearity. Here, we therefore propose to study how the latter can impact the previous analysis. For this, we take a simple model and introduce a cubic term in Eq. (1) such that the evolution equation is now

$$\frac{d^2\psi}{dt^2} + \frac{2}{\tau} \frac{d\psi}{dt} + \omega^2[1 + \epsilon \cos(2\omega t)](\psi - \alpha\psi^3) = 0. \quad (8)$$

The nonlinearity tends to saturate the oscillation amplitude and Eq. (8) admits two subharmonic oscillating limit cycles with phase difference of  $\pi$ , as shown in Fig. 4(a). Depending on the initial conditions, one or the other will be chosen in a similar fashion as in the linear case. The limit cycles are associated with constant complex amplitude  $A(t)$  and can take two values  $\pm A_c$  that correspond to the two possible phase states of the system. Convergence toward those fixed points in the complex plane replaces alignment of  $\vec{A}$  with  $\pm e_-$  in the linear case. As the problem is no longer linear, we will moreover consider the trajectories of  $A(t)$  in the complex plane, rather than only its phase as in Fig. 4(a).

We assume that the system ran for a long time before  $t = 0$  and that it reached a limit cycle. Adding a defect parameterized by  $\lambda$  will perturb the cycle, and the complex amplitude will start to move in the complex plane. After the perturbation, the system reaches one of its two limit cycles. Numerical simulations for different values of  $\lambda$  are shown in Fig. 4(b), with the forcing fixed to  $\epsilon = 0.03$ . Depending on the value of  $\lambda$ , a phase switch occurs or does not occur, which is associated, respectively, with nonzero or zero half winding around the origin. When  $\lambda$  spans different values, a family of trajectories is generated in the same manner as in the linear case.

The half-winding index  $Q$  is shown in Fig. 4(c) (upper panel) for different values of  $\lambda$  and goes abruptly from one value to the other for the specific value  $\lambda_c \approx 0.54\%$ . In terms of path, it is shown in Fig. 4(b) that close values of  $\lambda = 0.540\%$  and  $\lambda = 0.543\%$  can correspond to very different trajectories. As in the linear case, the transition is associated with a zero amplitude (middle panel). One can also compute the time for the system to converge back to its new limit cycle, and this time diverges at the transition (lower panel). Moreover, the scaling law  $T_c \sim \ln|\lambda - \lambda_c|$  predicted in the linear case still holds, as shown in the inset with a semilogarithmic plot. For  $\lambda \sim \lambda_c$ , the amplitude is very small during most of the transition between the limit cycles. The nonlinearity can

therefore be neglected during most of the dynamics, leaving the scaling law for the transition time insensitive to it.

Many works have investigated the switching between the stable states' bifurcation in the presence of noise [27,34]. It has been shown in particular that the system tends to escape through saddle points, which is exactly what we observe here. The critical trajectory associated to  $\lambda_c$  is tangent to  $\vec{e}_+$  when it goes toward the saddle point and tangent to  $\vec{e}_-$  when it escapes from it, generating an angular point at the saddle point, as shown in Fig. 4(b). The critical curve separates a different homotopy class for the trajectories. We would also like to mention that changing the type of defect would change the continuous family of trajectories that is generated, but not the physical features of the transitions (cancellation of field, divergence of the convergence time, etc.). The framework presented here can therefore be transposed to any other continuously parameterized family of defects.

### B. Impact of nonlinearity on transition diagrams

For now, it seems that apart from replacing eigenvectors by limit cycles to take into account amplitude saturation, nonlinearity may not significantly impact the physics of transition. This is actually not the case. Surprising consequences of nonlinearity are observed when one computes the transition diagram  $Q(\epsilon, \lambda)$ , shown in Fig. 4(d), that is completely different from the one shown in Fig. 2(d). First, it clearly breaks the symmetry between positive and negative values of detuning  $\lambda$ . Second, larger winding number is observed in those diagrams for negative detuning, but not for positive ones. Such large winding numbers were not observed in the linear regime and are therefore a striking signature of nonlinearities. It has also been verified that each transition of winding number is associated with field cancellation and convergence time divergence as in the linear case. Nevertheless, the values of  $(\lambda, \epsilon)$  at which the transition occurs are completely different from the linear case, as shown in Fig. 4(d).

Here, we briefly discuss the reasons for such differences between linear and nonlinear regimes. One can show that the evolution equation for the amplitude is of the form

$$\dot{A} + \frac{1}{\omega\tau}A = -\frac{3i\alpha\epsilon}{2}|A|^2A + \frac{i\epsilon}{4}A^*e^{2i\lambda(t)t}, \quad (9)$$

where  $\lambda(t) = \lambda$  for  $0 \leq t \leq T_\lambda$ , and zero otherwise. In the linear limit  $\alpha = 0$ , one can map this equation on another one that only depends on  $\lambda/\epsilon$  [28]. This indicates that the results in the linear case can only depend on this ratio, which is consistent with the results from the previous section. A similar argument predicts the antisymmetry  $\lambda \rightarrow -\lambda$  in the linear case. However, both of these symmetries break down in the presence of nonlinearity ( $\alpha \neq 0$ ). This is reminiscent of the different behaviors of parametric oscillators (subcritical or supercritical bifurcation) depending on the sign of the detuning [12,13]. Such analysis explains why the phase diagrams are different and nonsymmetric in the nonlinear case, but do not predict when the transition occurs. Such prediction requires a full treatment of the nonlinear problem, which appears very difficult to perform.

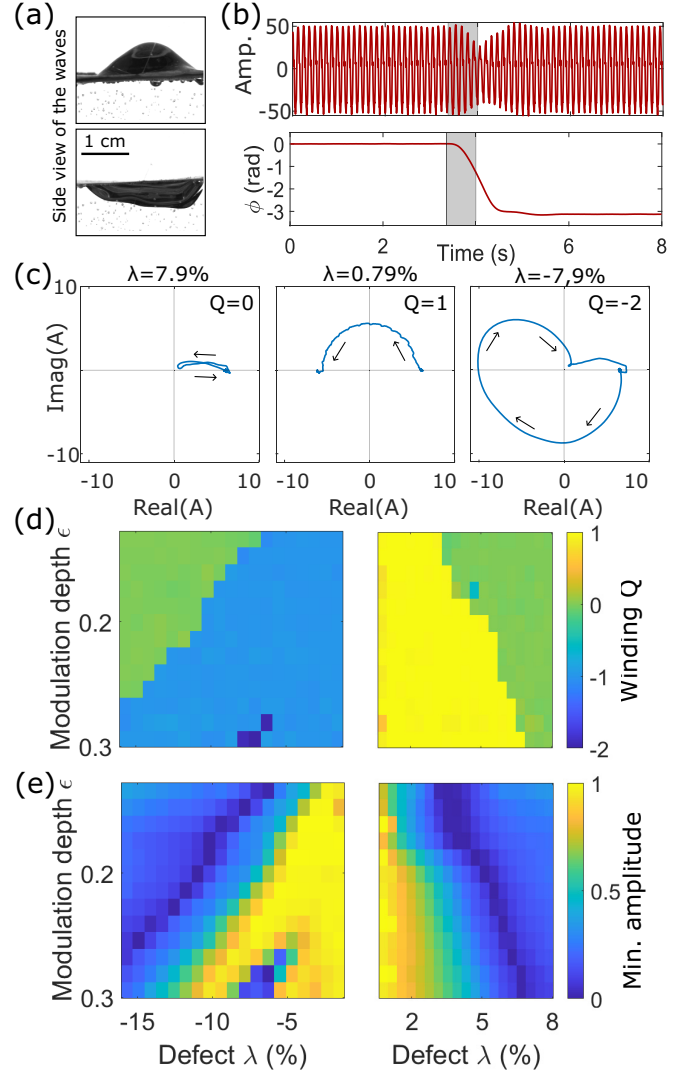


FIG. 5. Experimental measurement of transition diagram in the nonlinear case. (a) Pictures from the side of the parametrically excited water wave limit cycles with opposite phases. (b) Typical experimental measurement of wave amplitude (in arbitrary units) along time and its associated complex phase. The gray area materializes the time defect. (c)–(e) Complex amplitudes showing different half-winding values for fixed  $\epsilon = 0.29$ :  $Q = 0$  (right,  $\lambda = 7.9\%$ ),  $Q = 1$  (middle,  $\lambda = 0.79\%$ ),  $Q = -2$  (left,  $\lambda = -7.9\%$ ). (d) Experimental transition diagram of  $Q$  and (e) associated minimum amplitude of the wave field.

### C. Experimental observation

Last, we propose an experimental observation of a nonlinear transition diagram. We use the same experimental setup as before, for which the instability occurs for  $a \sim 1.4 \text{ m/s}^2$ , which corresponds to  $\epsilon_c \sim 0.12$  (see the Supplemental Material [28]). On the other hand, taking  $a$  typically greater than  $3.5 \text{ m/s}^2$  leads to unwanted phenomena such as water droplet ejection or water leaking on the floating sheet, limiting the maximal reachable forcing to  $\epsilon \sim 0.3$ . We perform wave amplitude measurement for various values of  $\epsilon$  and  $\lambda$  in order to obtain the complete transition diagram. Contrary to the linear case, we let the system reach its

saturated oscillation amplitude before introducing the temporal defect. This occurs within a few seconds for  $\epsilon > 0.13$ . Due to the high amplitude of the nonlinear waves, the previous demodulation method used to recover the wave amplitude could not be used. We therefore place a camera on the side and recover the wave amplitude using contrast analysis from raw pictures, as in Fig. 5(a). The typical measurement of the wave amplitude along time as well as the corresponding phase are shown in Fig. 5(b) [28]. Several examples of complex amplitude  $A(t)$  with different half-winding numbers associated to different values of  $\lambda$  are also shown in Fig. 5(c).

We performed systematic measurement of half-winding  $Q$  for different values of forcing  $\epsilon$  and detuning  $\lambda$ . The obtained transition diagram is shown in Fig. 5(d). It clearly exhibits distinct domains with different values of the winding index  $Q$ . We see, once again, the existence of large domains separated by critical curves. At those critical curves, the minimum amplitude of the field vanishes, as shown in Fig. 5(e), which is consistent with the previous analysis. However, a strong asymmetry exists between the positive and negative values of  $\lambda$ , which was not seen in the linear regime. Moreover, a larger winding index of  $-2$  has also been observed experimentally, as shown in Figs. 5(c) and 5(d). Although quite simple, the nonlinear model discussed above exhibits similar features. The domains in Figs. 4(d) and 5(d), moreover, look similar qualitatively, but could not be matched quantitatively. This

suggests that the full dynamic of Faraday waves is not entirely captured by Eq. (9), which was derived for small forcing.

## V. CONCLUSION

In this article, we have theoretically and experimentally studied how a system that exhibits a discrete number of limit cycles can (or cannot) switch from one to another by introducing continuously parameterized defects in the excitation. Both the linear and nonlinear cases have been discussed, and the difference between the two has been emphasized. Our results provide an example of a topological transition in a nonlinear time-varying system, and the topological index can be interpreted as a half-winding number of trajectories in phase space. All the predicted features of the transition have been observed experimentally using Faraday instability. The results presented in this article may find applications in the control of parametric oscillators or for robust bit flip in coherent Ising machines. It also paves the way toward the definition of new topological features in nonlinear or active systems that exhibit a finite number of limit cycles.

## ACKNOWLEDGMENTS

The authors acknowledge Herve Lissek for the loan of the shaker and the Swiss National Science Foundation Eccellenza Grant No. 181232 for financial support.

- 
- [1] D. C. Burnham and D. L. Weinberg, Observation of simultaneity in parametric production of optical photon pairs, *Phys. Rev. Lett.* **25**, 84 (1970).
  - [2] G. Milburn and D. F. Walls, Production of squeezed states in a degenerate parametric amplifier, *Opt. Commun.* **39**, 401 (1981).
  - [3] L.-A. Wu, M. Xiao, and H. J. Kimble, Squeezed states of light from an optical parametric oscillator, *J. Opt. Soc. Am. B* **4**, 1465 (1987).
  - [4] S. A. Akhmanov, A. I. Kovrigin, A. S. Piskarskas, V. V. Fadeev, and R. V. Khokhlov, Observation of parametric amplification in the optical range, *JETP Lett.* **2**, 191 (1965).
  - [5] J. A. Giordmaine and R. C. Miller, Tunable coherent parametric oscillation in LiNbO<sub>3</sub> at optical frequencies, *Phys. Rev. Lett.* **14**, 973 (1965).
  - [6] A. A. Grandi, S. Protière, and A. Lazarus, Enhancing and controlling parametric instabilities in mechanical systems, *Extreme Mech. Lett.* **43**, 101195 (2021).
  - [7] D. W. Carr, S. Evoy, L. Sekaric, H. G. Craighead, and J. M. Parpia, Parametric amplification in a torsional microresonator, *Appl. Phys. Lett.* **77**, 1545 (2000).
  - [8] D. Rugar and P. Grütter, Mechanical parametric amplification and thermomechanical noise squeezing, *Phys. Rev. Lett.* **67**, 699 (1991).
  - [9] K. L. Turner, S. A. Miller, P. G. Hartwell, N. C. MacDonald, S. H. Strogatz, and S. G. Adams, Five parametric resonances in a microelectromechanical system, *Nature (London)* **396**, 149 (1998).
  - [10] R. Berthet, A. Petrosyan, and B. Roman, An analog experiment of the parametric instability, *Am. J. Phys.* **70**, 744 (2002).
  - [11] M. Faraday, XVII. On a peculiar class of acoustical figures; and on certain forms assumed by groups of particles upon vibrating elastic surfaces, *Philos. Trans. R. Soc. London* **121**, 299 (1997).
  - [12] S. Douady, Experimental study of the Faraday instability, *J. Fluid Mech.* **221**, 383 (1990).
  - [13] S. Fauve, Pattern forming instabilities, in *Hydrodynamics and Nonlinear Instabilities*, Collection Alea-Saclay: Monographs and Texts in Statistical Physics, edited by C. Godrèche and P. Manneville (Cambridge University Press, Cambridge, 1998), pp. 387–492.
  - [14] G. d’Hardemare, A. Eddi, and E. Fort, Probing Floquet modes in a time periodic system with time defects using Faraday instability, *Europhys. Lett.* **131**, 24007 (2020).
  - [15] E. Lustig, Y. Sharabi, and M. Segev, Topological aspects of photonic time crystals, *Optica* **5**, 1390 (2018).
  - [16] E. Goto, The parametron, a digital computing element which utilizes parametric oscillation, *Proc. IRE* **47**, 1304 (1959).
  - [17] F. Sterzer, Microwave parametric subharmonic oscillators for digital computing, *Proc. IRE* **47**, 1317 (1959).
  - [18] S. Utsunomiya, K. Takata, and Y. Yamamoto, Mapping of Ising models onto injection-locked laser systems, *Opt. Express* **19**, 18091 (2011).
  - [19] T. Honjo, T. Sonobe, K. Inaba, T. Inagaki, T. Ikuta, Y. Yamada, T. Kazama, K. Enbutsu, T. Umeki, R. Kasahara, Ken-ichi Kawarabayashi, and H. Takesue, 100,000-spin coherent Ising machine, *Sci. Adv.* **7**, eabh0952 (2021).
  - [20] T. Inagaki, K. Inaba, R. Hamerly, K. Inoue, Y. Yamamoto, and H. Takesue, Large-scale Ising spin network based on degenerate optical parametric oscillators, *Nat. Photon.* **10**, 415 (2016).

- [21] Z. Wang, A. Marandi, K. Wen, R. L. Byer, and Y. Yamamoto, Coherent Ising machine based on degenerate optical parametric oscillators, *Phys. Rev. A* **88**, 063853 (2013).
- [22] P. L. McMahon, A. Marandi, Y. Haribara, R. Hamerly, C. Langrock, S. Tamate, T. Inagaki, H. Takesue, S. Utsunomiya, K. Aihara, R. L. Byer, M. M. Fejer, H. Mabuchi, and Y. Yamamoto, A fully programmable 100-spin coherent Ising machine with all-to-all connections, *Science* **354**, 614 (2016).
- [23] I. Mahboob and H. Yamaguchi, Bit storage and bit flip operations in an electromechanical oscillator, *Nat. Nanotechnol.* **3**, 275 (2008).
- [24] M. Frimmer, T. L. Heugel, Ž. Nosan, F. Tebbenjohanns, D. Hälg, A. Akin, C. L. Degen, L. Novotny, R. Chitra, O. Zilberberg, and A. Eichler, Rapid flipping of parametric phase states, *Phys. Rev. Lett.* **123**, 254102 (2019).
- [25] D. Luchinsky, S. Beri, R. Mannella, P. McClintock, and I. Khovanov, Optimal fluctuations and the control of chaos, *Intl. J. Bifurcat. Chaos* **12**, 583 (2002).
- [26] S. Boccaletti, C. Grebogi, Y. C. Lai, H. Mancini, and D. Maza, The control of chaos: Theory and applications, *Phys. Rep.* **329**, 103 (2000).
- [27] S. Beri, R. Mannella, D. G. Luchinsky, A. N. Silchenko, and P. V. E. McClintock, Solution of the boundary value problem for optimal escape in continuous stochastic systems and maps, *Phys. Rev. E* **72**, 036131 (2005).
- [28] See Supplemental Material at <http://link.aps.org/supplemental/10.1103/PhysRevE.109.054204> for detailed computation, study of the equation invariance, and full description of experimental apparatus and measurement.
- [29] L. Papariello, Parametric resonance in classical and quantum systems, Ph.D. thesis, ETH Zurich, 2018.
- [30] N. Batra and G. Sheet, Physics with coffee and doughnuts, *Resonance* **25**, 765 (2020).
- [31] T. Kitagawa, E. Berg, M. Rudner, and E. Demler, Topological characterization of periodically driven quantum systems, *Phys. Rev. B* **82**, 235114 (2010).
- [32] R. Fleury, A. B. Khanikaev, and A. Alù, Floquet topological insulators for sound, *Nat. Commun.* **7**, 11744 (2016).
- [33] S. Wildeman, Real-time quantitative schlieren imaging by fast Fourier demodulation of a checkered backdrop, *Expt. Fluids* **59**, 97 (2018).
- [34] A. N. Silchenko, S. Beri, D. G. Luchinsky, and P. V. E. McClintock, Fluctuational transitions through a fractal basin boundary, *Phys. Rev. Lett.* **91**, 174104 (2003).